Optical Properties of Metal–Molybdenum Disulfide Hybrid Nanosheets and Their Application for Enhanced Photocatalytic Hydrogen Evolution

Lei Yang,[†] Ding Zhong,[‡,▽] Jingyu Zhang,[§] Zhiping Yan,[†] Shaofeng Ge,[‡,▽] Pingwu Du,[†,*] Jun Jiang,[⊥] Dong Sun,[‡,▽,*] Xiaojun Wu,[†] Zhiyong Fan,[∥] Shadi A. Dayeh,[#] and Bin Xiang[†,*]

[†]Department of Materials Science & Engineering, CAS key Lab of Materials for Energy Conversion, University of Science and Technology of China, Hefei, Anhui 230026, P. R. China, [‡]International Center for Quantum Materials, Peking University, Beijing 100871, China, [§]Molecular Foundry, Lawrence Berkeley National Laboratory, 1 Cyclotron Road, Berkeley, California 94720, United States, [⊥]Department of Chemical Physics, University of Science and Technology of China, Hefei, Anhui 230026, P. R. China, [∥]Department of Electronic, and Computer Engineering, Hong Kong University of Science and Technology Hong Kong SAR, China, [#]Department of Electrical and Computer Engineering, University of California, San Diego, California 92093, United States, and [▽]Collaborative Innovation Center of Quantum Matter, Beijing, 100871,China

ABSTRACT Limited control over charge recombination between photogenerated charge carriers largely hinders the progress in photocatalysis. Here, we introduce metal nanoparticles (Cr, Ag) to the surface of MoS_2 nanosheets by simple synthetic means creating a hybrid metal–MoS_2 nanosheet system with well-defined metal/semiconductor interfaces. We demonstrate that this hybrid nanosheet structure is capable of decoupling light absorption, primarily in MoS_2, and carrier separation, across the metal–MoS_2 heterostructure leading to drastic quenching of recombination between photogenerated carriers in MoS_2, as proven by absorptance, photoluminescence, and ultrafast pump-probe spectroscopy. The photocatalytic activity in the hybrid system is also improved, which further shows excellent stability against photocorrosion.

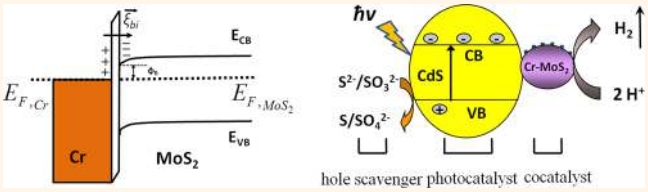

KEYWORDS: MoS_2 · hybrid nanosheets · interface · carrier recombination · pump probe · photocatalysis

The photocatalytic splitting of water using solar energy is an attractive way to produce clean and recyclable hydrogen fuel.[1−6] Semiconductor-based catalytic systems have been investigated in the past few years.[7−15] For instance, the introduction of lithium intercalation as interlayer species in vertical MoS_2 sheets has been demonstrated to modify the chemical potential of Li_xMoS_2, which in turn tunes the catalytic performance of MoS_2 in the electrocatalytic hydrogen production.[8] However, in photocatalytic hydrogen production, the energy conversion efficiencies, limited by charge recombination and inefficient catalytic reduction and oxidation reactions,[16] are still low for practical applications. Cocatalysts for both oxidation and reduction reactions have received tremendous attention to improve semiconductor-based catalytic activities.[16] Noble metals that decrease the activation energy[17,18] have traditionally been the popular candidates for efficient catalytic reduction cocatalysts. But the high cost of noble metals prompts the pursuit of alternative cocatalysts with comparable efficiency. Recently, MoS_2 nanostructures have been extensively explored in photocatalysis research activities due to its distinctive electronic, optical, and catalytic properties.[19] Its stability against the photocorrosion in solution is another attractive and desired attribute for solar photoelectrochemical applications.[20,21] The antibonding state formed from an interaction between molybdenum d_z^2, and sulfur p_z orbital at the top of the valence band is believed to be responsible for the high stability of MoS_2 in solution.[22] As a cocatalyst, MoS_2 has been properly combined with CdS for photocatalytic hydrogen

* Address correspondence to binxiang@ustc.edu.cn, dupingwu@ustc.edu.cn, sundong@pku.edu.cn.

Received for review April 2, 2014 and accepted June 2, 2014.

Published online 10.1021/nn501807y

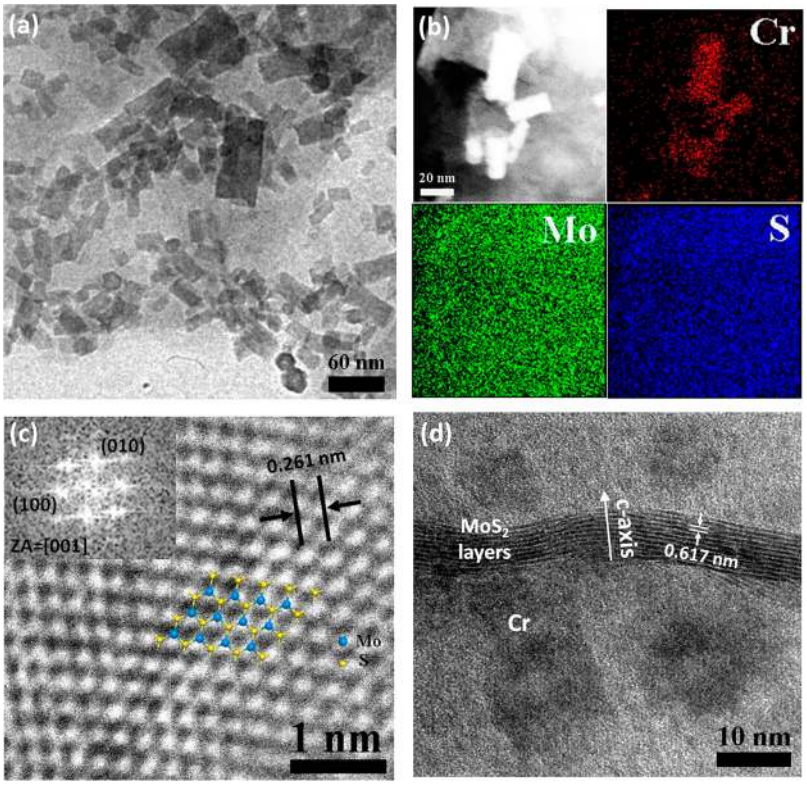

Figure 1. (a) TEM image of the Cr−MoS_2 hybrid nanosheets. (b) EDS mapping of the Cr−MoS_2 hybrid nanosheets to confirm the chemical compositions. (c) HRTEM image of in-plane MoS_2 nanosheets. The lattice is composed of hexagonal rings alternating molybdenum and sulfur sites as is illustrated by the overload color spheres. The inset shows the corresponding fast Fourier transformation (FFT). The zone axis is along [001] direction. (d) Cross-sectional HRTEM image of the Cr−MoS_2 hybrid nanosheets. The strips are the layers of MoS_2, and the distance between each layer is ~0.617 nm. The rectangular features are the Cr nanoparticles with a diameter of 15 nm.

evolution under visible light illumination.[23] However, the progress in hydrogen evolution reactions (HERs) is still hindered largely by the limited control over charge recombination between photogenerated electrons, and holes.[24]

To increase the photogenerated carrier separation and reduce the electron-hole recombination process for HER applications, we introduced in this work metal nanoparticles (Cr, Ag) onto the MoS_2 nanosheet surface by a solution-based method to act as trapping sites for photogenerated electrons. A metal/semiconductor configuration with well-defined interface in the Cr−MoS_2 hybrid nanosheets has been demonstrated through a cross-sectional high-resolution transmission electron microscope (HRTEM) characterization. Reduction of photogenerated charge carrier recombination in the Cr−MoS_2 configuration has been demonstrated by ultrafast pump-probe spectroscopy and by the dramatic quenching of the photoluminescence intensity of Cr−MoS_2 hybrid structures, which is owed to decoupling of light absorption in the MoS_2 nanosheets and their separation across the Cr−MoS_2 hybrid nanosheet system. Finally, the Cr−MoS_2 hybrid nanosheets were utilized as cocatalyst in a HER, which exhibited higher catalytic performance than MoS_2 nanosheets alone.

RESULTS AND DISCUSSION

A hydrothermal method was employed for the synthesis of the MoS_2 nanosheets (Supporting Information Figure S1a). X-ray diffraction (XRD) was employed to study the crystal structure of the as-synthesized products. The XRD pattern of the as-synthesized nanosheets (Supporting Information Figure S1) with the lines indexed according to JCPDF card number 37-1492 corresponds to the hexagonal structure of MoS_2.[25,26] The nanosheets roll up and form into continuous three-dimensional (3D) networks (inset in Supporting Information Figure S1c). The low magnification TEM image in Figure 1a shows the morphology of the resulting Cr−MoS_2 hybrid nanosheets. The size of the coated Cr nanoparticles has a range from 10 to 100 nm. The chemical composition of the Cr−MoS_2 hybrid nanosheets is characterized by energy dispersive X-ray spectroscopy (EDS) mapping as shown in Figure 1b validating the existence of variable Cr nanoparticle sizes stop the MoS_2 sheets. Figure 1c shows the HRTEM image of the basal plane of the MoS_2 nanosheets with its corresponding fast Fourier transformation (FFT, inset of Figure 1c). The noted (100) and (010) atomic plane distance is measured to be ~2.6 Å. Figure 1d shows the cross-sectional HRTEM image of hybrid Cr−MoS_2 nanosheets with an

interlayer distance of ~6.17 Å. The cross-sectional HRTEM characterization confirmed that the Cr nanoparticles only stay on the surface of outermost layers of the MoS_2 nanosheets and none were observed between its interlayers (Figure 1d). As observed in the high resolution basal-plane and cross-sectional TEM images, the continuous lattice fringes imply defect-free as-grown MoS_2 nanosheets.

The value of Cr work function is 4.5 eV and that reported of MoS_2 work function is ~5.1 eV.[27] A qualitative sketch of the ideal energy band-edge at thermal equilibrium is sketched in Figure 2a. The work function difference between Cr and MoS_2 leads to electron transfer from Cr into the lower energy states in MoS_2 through a thin interfacial barrier layer (Figure 2a) and causing a built-in electric field, ξ_{bi}, directed from Cr toward the MoS_2 layer. The electron energy barrier height, ϕ_B, is 0.6 eV (ideal case) and is generally influenced by the interface state density at the Cr−MoS_2 metallurgical contact. This relatively large barrier height and the correspondent electric field are responsible for efficient separation of photogenerated carriers in the Cr−MoS_2 hybrid nanosheets as demonstrated below. Figure 2b shows the photoluminescence (PL) spectra with a peak at 693 nm (1.79 eV) observed in the MoS_2 nanosheets at room temperature. This peak is assigned to a direct transition between the top valence band K point and the bottom conduction band K point in the Brillouin zone.[28] The shift of the PL peak from 1.9 eV (monolayer MoS_2) to 1.79 eV is attributed to the variation in the number of layers of MoS_2. With the introduction of Cr to MoS_2 nanosheets, the intensity of photoluminescence is drastically quenched as can be seen from the red spectrum shown in Figure 2b due to the efficient charge separation in the presence of ξ_{bi} at Cr−MoS_2 junction. Similar quenching behavior is also observed in Ag-MoS_2 hybrid nanosheets from the blue spectrum in Figure 2b.

The absorption spectra of metal (Cr, Ag)−MoS_2 hybrid nanosheets demonstrate distinctively new behavior (Figure 2c). In the absorption spectra of MoS_2 nanosheets, the first absorption edge was observed at ~700 nm, which is associated with a direct transition at the K point of the Brillouin zone.[29] On the short-wavelength side of this threshold, peaks A (660 nm, 1.88 eV) and B (605 nm, 2.05 eV) are assigned to excitonic transitions at the K point of the Brillouin zone,[30] which are in-plane polarized transitions. Due to the spin-orbit splitting at the top of the valence band at K point, there is an energy separation of 0.17 eV between those two peaks. A second threshold appears at ~500 nm in the MoS_2 nanosheet spectrum, which is attributed to a direct transition from deeper valence band to the conduction band. On the high-energy side of this threshold, a shoulder C (410 nm, 3.02 eV) is observed, which is associated with a direct excitonic

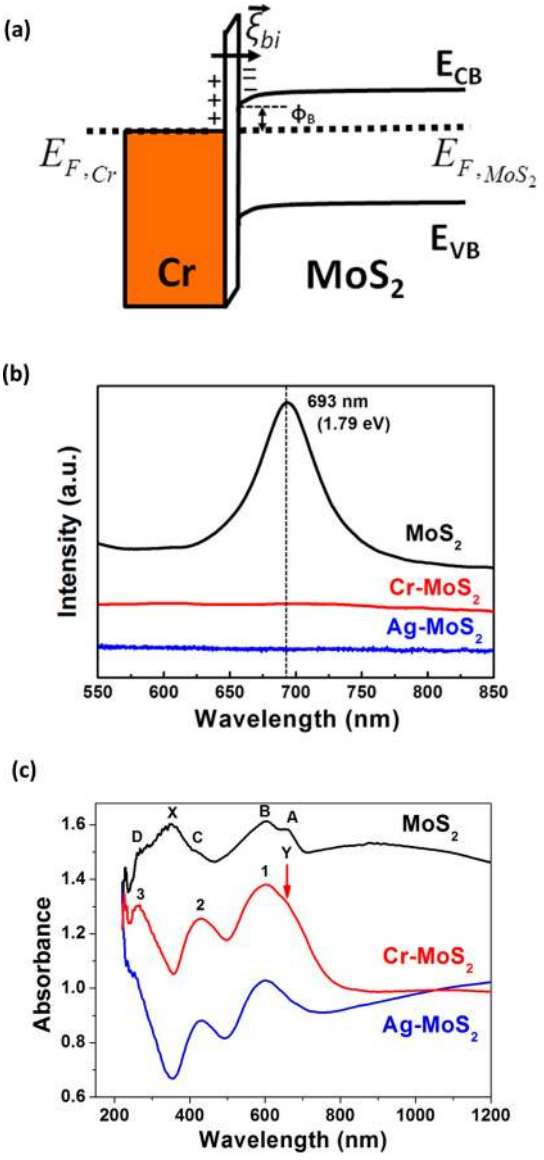

Figure 2. (a) Energy band-edge alignment of Cr−MoS_2 hybrid structure. ϕ_{Cr} and ϕ_{MoS2} are the work functions of the Cr nanoparticles and MoS_2, respectively. $E_{F,Cr}$ and $E_{F,\ MoS2}$ are the Fermi Levels of Cr and MoS_2, respectively. ϕ_B is the electron barrier potential in the hybrid Cr−MoS_2 system. E_{CB} and E_{VB} are the conduction and valence band-edges of MoS_2, respectively. A thin interfacial layer is inserted between Cr and MoS_2 to indicate a nonepitaxial contact. (b) Photoluminescence spectra of the MoS_2, Cr−MoS_2, and Ag−MoS_2 nanosheets. (c) Absorption spectra of the MoS_2, Cr−MoS_2, and Ag−MoS_2 nanosheets.

transition at M point of the Brillouin zone.[30] Feature X observed at 350 nm (3.54 eV) in the spectrum, correlates to a c-axis polarized transition.[31,32] The spectra also provides better resolution of high energy feature D (268 nm). The sharp peak at the higher energy side of feature D is out of the spectrometer range, which is not included in our data analysis. Peaks 1, 2, and 3 observed in the spectrum of Cr−MoS_2 nanosheets have wavelengths of 605, 430, 268 nm, respectively. Compared to the spectral features of MoS_2 nanosheets, it indicates a one-to-one correlation between Cr−MoS_2 and MoS_2

spectra. Thus, peaks 1, 2, and 3 are well-defined. Feature Y (660 nm, 1.88 eV), which appears as a shoulder in the Cr−MoS_2 spectrum, is associated with the peak A of MoS_2 nanosheets. The most interesting observation is that any peak associated with peak X disappears in the Cr−MoS_2 spectrum and a new absorption edge appears at ~350 nm in the Cr−MoS_2 spectrum. This effect is due to a spectral interference appearing after introducing the Cr nanoparticles to MoS_2 nanosheets. By introducing Cr nanoparticles onto the surface of MoS_2 nanosheets, along the MoS_2 *c*-axis, Cr could interact with surface sulfur to form new hybrid orbital sticking out of MoS_2 nanosheet plane. Therefore, it modifies the density of the *c*-polarized exciton states in the original MoS_2 nanosheets, resulting in preventing the observation of the peak X related excitonic transitions. In the spectra of Cr−MoS_2 nanosheets, the spin-orbital splitting induced energy separation between peak 1 and Y is the same as that of MoS_2 nanosheets. It reveals that the strong interaction between Cr nanoparticles and MoS_2 nanosheets has less influence on the in-plane spin-orbit interaction at the K point of the Brillouin zone in MoS_2 nanosheets. Similar results are observed in the Ag−MoS_2 hybrid nanosheets as shown in Figure 2c. Compared with MoS_2, metal−MoS_2 hybrid fairly preserves the high light absorption capability. The hybridization in the bonding states of metal and S with strong covalent interaction favors the MoS_2 stability against photocorrosion.[30]

To verify the effect of the well-defined interface to the recombination time of the photogenerated carriers, we carried out ultrafast pump-probe measurements to capture the carrier dynamics in MoS_2 and Cr−MoS_2 nanosheets. In these experiments, a 60 fs 250-kHz amplified Ti:sapphire laser at 800 nm was split into two arms, both focused on a 2 mm sapphire plate to generate white light supercontinuum. Two 10 nm bandpass filters were used to filter the 633 nm (1.964 eV) as pump and 670 nm (1.855 eV) as probe for the pump-probe measurement. As inferred from Figure 2c, the 633 nm pump is slightly above the A-exciton energy, while the 670 nm probe is in resonance with the A-exciton of both Cr−MoS_2 and MoS_2. The absorption edge of Cr is at ~500 nm (Supporting Information Figure S2), suggesting that Cr nanoparticles are not involved in the pumping effect (633 nm pump). Hence, the pump laser only excites electron-hole pairs from the MoS_2 nanosheets. After the excitation of the pump pulse, the modification of carrier distribution induced by the pump pulse excitation results in perturbation of the probe reflection intensity. The pump induced probe reflection change, ΔR, was recorded as a function of pump and probe delay by a Si photodetector and lock-in amplifier referenced to 5.7-kHz mechanically chopped pump. Both pump and probe photons are focused onto the sample through a

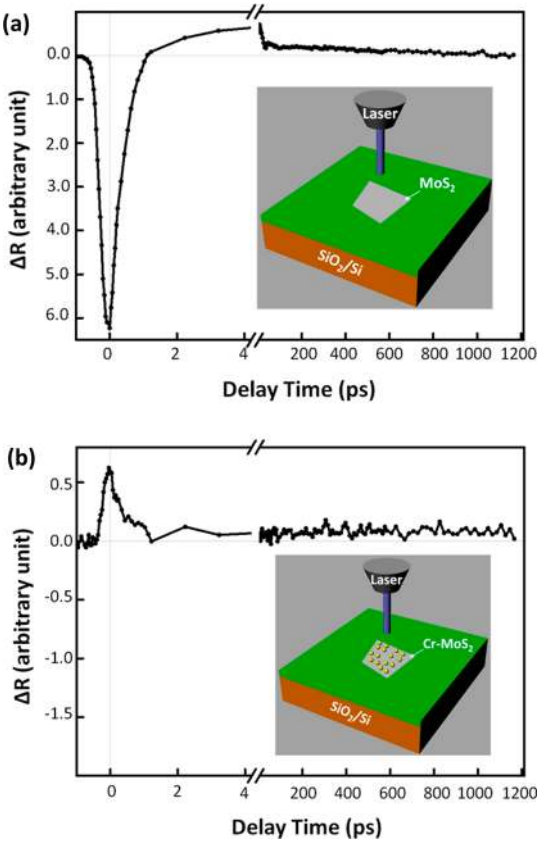

Figure 3. Ultrafast pump-probe spectroscopy with 633 nm (1.964 eV) as pump and 670 nm (1.855 eV) as probe. (a) Pump induced differential refection spectrum of MoS_2 nanosheets. Inset pump-probe experiment sketch of single piece of MoS_2 nanosheet. (b) Pump induced differential reflection spectrum of Cr−MoS_2 hybrid nanosheets. Inset pump-probe experiment sketch of single piece of Cr−MoS_2 hybrid nanosheet.

40× objective, and the probe spot size is estimated to be below 2 μm with pump spot size slightly larger. The temporal resolution is about 200 fs, and the pump fluence is kept around 4×10^{14} photons/cm^2.

Figure 3 shows representative differential reflection spectra of MoS_2 and Cr−MoS_2 nanosheets. The MoS_2 nanosheet shows negative ΔR around time zero due to initial excitation of A exciton by the pump pulse. When the exciton distribution changes due to relaxation to quasi-equilibrium, lower energy state, ionized or recombined, the sign and amplitude of ΔR evolves. Within only 1 ps delay, the signal switches to positive and then it has a long decay time over ~600 ps to zero. In contrast, the Cr−MoS_2 nanosheet shows positive ΔR at time zero and then the positive ΔR decays to zero gradually within only 2 ps. The ΔR response around time zero usually comes from multiple effects when many body effect dominates the response for a highly excited nonequilibrium state;[33−35] thus, it is not the focus of this paper. Probable reasons of this ΔR sign difference between Cr−MoS_2 and MoS_2 nanosheet can be due to the thickness difference of MoS_2 or slightly modulated electronic band structure of Cr−MoS_2 as

referred from the absorption spectra in Figure 2c. The subsequent decay tail of positive ΔR to zero is the focus of our studies. Since the pump photon energy is only 100 meV above the A-exciton energy, the initial vibrational relaxation to ground state should be fast and on the order of several ps, so the long decay tail over 600 ps in MoS_2 nanosheet corresponds to the interband recombination time of pump excited exciton in MoS_2 as studied by extensive previous pump probe measurements.[34,35] The decay time decreases significantly to less than 2 ps in Cr−MoS_2 samples. This tremendous change of decay time in Cr−MoS_2 can be elucidated by a transfer of the pumped electrons from MoS_2 to Cr across their interface due to the built-in electric field ξ_{bi} as discussed above. The photogenerated carriers are immediately (within 2 ps) separated by this built-in electric field and most of the generated electrons are injected to Cr nanoparticle side, thus no longer contribute to ΔR. This indicates that a very short lifetime of the photogenerated electrons was detected in the pump-probe measurement. A similar phenomenon due to the Au nanoparticles coating has been previously reported in the MoS_2 nanoclusters.[30] The pump-probe measurement suggests that the well-defined interface between Cr and MoS_2 nanosheets exerts a profound impact on electron transfer behavior, which is likely to provide a special configuration of Cr−MoS_2 as cocatalyst applied in HER.

To assess the catalytic performance, the Cr−MoS_2 nanosheets were utilized as a cocatalyst combined with CdS photocatalyst (details in Supporting Information) for photocatalytic HER. With the same loading, the Cr−MoS_2 nanosheets exhibit higher catalytic performance than MoS_2 nanosheets alone for hydrogen production. As shown in Figure 4a, the hydrogen yield is enhanced by Cr−MoS_2 hybrid nanosheets than by MoS_2 nanosheets alone. The average rate of photocatalytic hydrogen evolution is 18 000 $\mu mol \cdot g^{-1} \cdot h^{-1}$ in MoS_2. With the hybrid configuration of Cr−MoS_2, the average rate of hydrogen evolution is increased to 38 000 $\mu mol \cdot g^{-1} \cdot h^{-1}$. The MoS_2 nanosheets were also coated by Ag nanoparticles to build up the Ag−MoS_2 interfaces. Similar absorption results were obtained in the Ag−MoS_2 hybrid configurations. Significant enhancement is achieved for photocatalytic HER in the case of Ag−MoS_2 as the cocatalyst, with an average rate of 107 000 $\mu mol \cdot g^{-1} \cdot h^{-1}$, which is 6 times higher than MoS_2 alone. The improved catalytic performance of Ag−MoS_2 hybrid nanosheets (Figure 4a) is attributed to the presence of a larger ξ_{bi} for the case of Ag−MoS_2 when compared to that of Cr−MoS_2 due to the larger Ag work function than that of Cr. Thus, photogenerated electrons are easier to be separated and trapped in the Ag nanoparticles for the Ag−MoS_2 hybrid structures resulting in higher hydrogen production levels than in Cr−MoS_2 hybrid nanosheets. Stability is another important issue for a

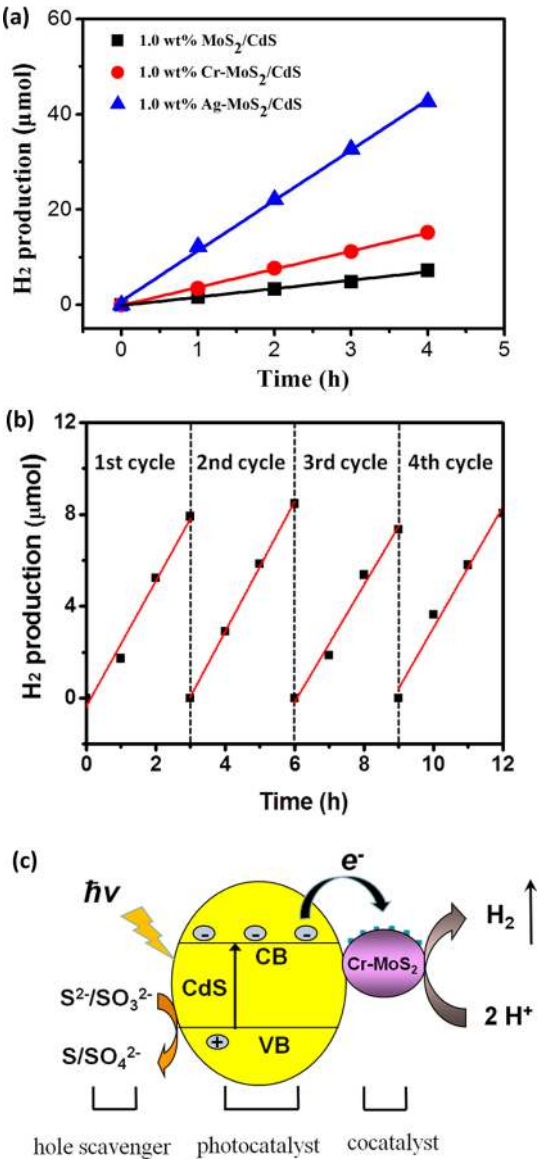

Figure 4. (a) The hydrogen production as a function of irradiation time. As cocatalysts combined with photocatalyst of CdS, the plots represent 1.0 wt % Cr−MoS_2 (in red), 1.0 wt % Ag−MoS_2 (in blue), and 1.0 wt % MoS_2 (in black). (b) Stable catalytic performance of Cr−MoS_2 hybrid nanosheets as cocatalyst in the HER demonstrating the significant stability of hydrogen production even after 12 h illumination. (c) Schematic illustration of photogenerated carrier transfer in a HER utilizing Cr−MoS_2 hybrid nanosheets as cocatalyst.

cocatalyst applied in catalytic reactions. Figure 4b shows the amount of hydrogen production under different reaction cycles, which shows linear dependence on irradiation time. The reaction system was evaluated every 3 h for one cycle. Even after 12 h, the reaction rate has no evident decrease. This level of performance stability indicates that the Cr−MoS_2 hybrid configuration possesses a novel feature to prevent photocorrosion. With the introduction of metal nanoparticles, the well-defined interface between metal and MoS_2 acts as electron sink for trapping the photogenerated electrons and dramatically

decreasing the carrier recombination processes in MoS_2 (Figure 4c). With extensively suppressing the electron-hole recombination processes, more photogenerated carriers are involved in HER instead of depletion by recombination. As a result, the catalytic performance of the metal−MoS_2 hybrid nanosheets as cocatalysts has been evidently improved in HERs. The peculiar interface configuration in metal−MoS_2 hybrid nanosheets can be used to tailor the electrical properties of the hybrid structures and promote the catalytic performance in HER.

CONCLUSIONS

In conclusion, we have successfully achieved high yield of Cr−MoS_2 and Ag−MoS_2 hybrid nanosheets by using solution-based methods for improved hydrogen photocatalytic production. Cross-sectional HRTEM characterization validated the presence of the metal/semiconductor configuration with well-defined interface in the Cr−MoS_2 nanosheets. The carrier dynamics study indicated that the coated Cr nanoparticles can be considered as trapping sites to reduce the photogenerated electron−hole recombination in MoS_2 nanosheets. Due to the trapping effect, the intensity of the photoluminescence of Cr−MoS_2 hybrid nanosheets has been extensively quenched. As cocatalysts, the Cr−MoS_2 hybrid nanosheets with a well-defined interface exhibit higher catalytic performance in HER compared to MoS_2 nanosheets alone. We also achieved similar behavior in Ag−MoS_2 hybrid nanosheets. These advances in chemically synthesized metal−MoS_2 hybrid structures provide a general strategy to overcome the limitation of carrier recombination in photocatalytic device applications.

METHODS

Synthesis of the MoS_2 Nanosheets. The MoS_2 nanosheets were successfully synthesized *via* hydrothermal method. A total of 3 mmol MoO_3 (The Company of Colloid Chemical, China) and 9 mmol of KSCN (Sinopharm Chemical reagent Co. Ltd, China) were dissolved in 80 mL of distilled water, and then 0.28 mL of HCl (Sinopharm Chemical Reagent Co. Ltd, China) with a concentration of 12.5 mol/L was added into the reaction solution under violent stirring for 12 h. The resulting solution was then transferred into a 100 mL Teflon-lined stainless autoclave, which was then sealed tightly and kept at 240 °C for 24 h in the oven. Then, the autoclave was cooled to room temperature in ambient conditions. The resulting products were filtered; washed with distilled water, absolute ethanol (Sinopharm Chemical reagent Co. Ltd, China) for 3 times, respectively; and dried in vacuum at 60 °C for 6 h.

Synthesis of Cr−MoS_2 Hybrid Nanosheets. A total of 1.6 mmol CTAB ($(C_{16}H_{33}(CH_3)_3)$ NBr) (Sinopharm Chemical Reagent Co. Ltd, China) and 0.04 mmol $Cr(NO_3)_3$ (Sinopharm Chemical Reagent Co. Ltd, China) were dissolved in 80 mL of distilled water with violent stirring. Then, 2 mg of MoS_2 nanosheets was dispersed in the above solution. A total of 3.2 mL of aqueous solution of ascorbic acid ($C_6H_8O_6$) (Sinopharm Chemical Reagent Co. Ltd, China) with the concentration of 50 mM and 3.2 mL of aqueous solution of 0.5 M NaOH (Sinopharm Chemical Reagent Co. Ltd, China) were added with mild shaking sequentially. After 1 h, the reaction solution was centrifuged for 10 min at 6000 rpm. The resulting products were filtered; washed with distilled water, absolute ethanol (Sinopharm Chemical reagent Co. Ltd, China) for several times, respectively; and dried in vacuum at 60 °C for 6 h for further characterization.

Synthesis of Ag−MoS_2 Hybrid Nanosheets[36]. A total of 1.6 mmol CTAB ($(C_{16}H_{33}(CH_3)_3)$ NBr) (Sinopharm Chemical Reagent Co. Ltd, China) and 0.008 mmol $AgNO_3$ (Sinopharm Chemical Reagent Co. Ltd, China) were dissolved in 80 mL of distilled water with violent stirring. Then, 2 mg of MoS_2 nanosheets was dispersed in the above solution. A total of 0.64 mL of aqueous solution of ascorbic acid ($C_6H_8O_6$ (Sinopharm Chemical Reagent Co. Ltd, China) with a concentration of 50 mM, 0.064 mL of aqueous solution of 0.5 M NaOH (Sinopharm Chemical Reagent Co. Ltd, China), and 0.5 mL of ice-water cooled aqueous solution of 100 mM $NaBH_4$ were added with mild shaking sequentially. After 10 min, the reaction solution was centrifuged for 10 min at 6000 rpm. The resulting products were filtered; washed with distilled water, absolute ethanol (Sinopharm Chemical Reagent Co. Ltd, China) for several times, respectively; and dried in vacuum at 60 °C for 6 h for further characterization.

Photocatalytic Hydrogen Evolution. The photocatalytic hydrogen evolution experiments were performed in a 50 mL flask at ambient temperature using a 300 W Xe lamp equipped with UV cut off filter (λ > 420 nm). Hydrogen gas was measured by gas chromatography (SP-6890, nitrogen as a carrier gas) equipped with thermal conductivity detector (TCD). In a typical photocatalytic experiment, 10 mg of the photocatalyst Cr−MoS_2−CdS sample (1 wt % Cr−MoS_2), MoS_2−CdS sample (1 wt % MoS_2), or Ag−MoS_2−CdS sample (1 wt % Ag−MoS_2) was mixed with 0.25 M Na_2S and 0.35 M Na_2SO_3 by ultrasonication for 10 min. Before each experiment, the suspension was purged with nitrogen for 15 min to remove air. During the photocatalytic reaction, the reactor was tightly sealed to avoid a gas exchange.

Conflict of Interest: The authors declare no competing financial interest.

Acknowledgment. This work was supported by National Natural Science Foundation of China (NSFC) (21373196, 11274015 and 21271166), the Recruitment Program of Global Experts, and the Fundamental Research Funds for the Central Universities (WK2060140014 and WK2340000050), National Basic Research Program of China (2012CB921300 and 2014CB920900), the Specialized Research Fund for the Doctoral Program of Higher Education of China (20120001110066), and a faculty start-up research grant for S.A.D. at UC San Diego.

Supporting Information Available: Schematic illustrations of the synthesis of MoS_2 hybrid nanosheets, XRD, 3D network morphology of MoS_2 nanosheets and simulated absorption spectrum of chromium. This material is available free of charge *via* the Internet at http://pubs.acs.org.

REFERENCES AND NOTES

1. Khaselev, O.; Turner, J. A. A Monolithic Photovoltaic-Photoelectrochemical Device for Hydrogen Production *via* Water Splitting. *Science* **1998**, *280*, 425–427.
2. Mor, G. K.; Shankar, K.; Paulose, M.; Varghese, O. K.; Grimes, C. A. Enhanced Photocleavage of Water Using Titania Nanotube Arrays. *Nano Lett.* **2005**, *5*, 191–195.
3. Qiu, Y.; Leung, S.; Zhang, Q.; Hua, B.; Lin, Q.; Wei, Z.; Tsui, K.; Zhang, Y.; Yang, S.; Fan, Z. Efficient Photoelectrochemical Water Splitting with Ultra-thin Film of Hematite on Three-Dimensional Nanophotonic Structures. *Nano Lett.* **2014**, *14*, 2123–2129.
4. Lin, Y. J.; Battaglia, C.; Boccard, M.; Hettick, M.; Yu, Z. B.; Ballif, C.; Ager, J. W.; Javey, A. Amorphous Si Thin Film

Based Photocathodes With High Photovoltage for Efficient Hydrogen Production. *Nano Lett.* **2013**, *13*, 5615–5618.
5. Osterloh, F. E. Inorganic Materials as Catalysts for Photochemical Splitting of Water. *Chem. Mater.* **2008**, *20*, 35–54.
6. Yin, Z. Y.; Chen, B.; Bosman, M.; Cao, X. H.; Chen, J. Z.; Zheng, B.; Zhang, H. Au Nanoparticle-Modified MoS_2 Nanosheet-Based Photoelectrochemical Cells for Water Splitting. *Small* **2014**, 10.1002/smll.201400124.
7. Yin, Z. Y.; Wang, Z.; Du, Y. P.; Qi, X. Y.; Huang, Y. Z.; Xue, C.; Zhang, H. Full Solution-Processed Synthesis of All Metal Oxide-Based Tree-like Heterostructures on Fluorine-Doped Tin Oxide for Water Splitting. *Adv. Mater.* **2012**, *24*, 5374–5378.
8. Wang, H.; Lu, Z.; Xu, S.; Kong, D.; Cha, J. J.; Zheng, G.; Hsu, P.-C.; Yan, K.; Bradshaw, D.; Prinz, F. B.; *et al.* Electrochemical Tuning of Vertically Aligned MoS_2 Nanofilms and Its Application in Improving Hydrogen Evolution Reaction. *Proc. Natl. Acad. Sci. U.S.A.* **2013**, *110*, 19701–19706.
9. Liang, Y.; Li, Y.; Wang, H.; Zhou, J.; Wang, J.; Regier, T.; Dai, H. Co_3O_4 Nanocrystals on Graphene as a Synergistic Catalyst for Oxygen Reduction Reaction. *Nat. Mater.* **2011**, *10*, 780–786.
10. Zou, Z.; Ye, J.; Sayama, K.; Arakawa, H. Direct Splitting of Water under Visible Light Irradiation with an Oxide Semiconductor Photocatalyst. *Nature* **2001**, *414*, 625–627.
11. Hoffmann, M. R.; Martin, S. T.; Choi, W.; Bahneman, D. W. Environmental Applications of Semiconductor Photocatalysis. *Chem. Rev.* **1995**, *95*, 69–96.
12. Maeda, K.; Teramura, K.; Lu, D.; Takata, T.; Saito, N.; Inoue, Y.; Domen, K. Photocatalyst Releasing Hydrogen from Water. *Nature* **2006**, *440*, 295–295.
13. Hu, J.-S.; Ren, L.-L.; Guo, Y.-G.; Liang, H.-P.; Cao, A.-M.; Wan, L.-J.; Bai, C.-L. Mass Production and High Photocatalytic Activity of ZnS Nanoporous Nanoparticles. *Angew. Chem.* **2005**, *117*, 1295–1299.
14. Baeck, S.-H.; Choi, K.-S.; Jaramillo, T. F.; Stucky, G. D.; McFarland, E. W. Enhancement of Photocatalytic and Electrochromic Properties of Electrochemically Fabricated Mesoporous WO_3 Thin Films. *Adv. Mater.* **2003**, *15*, 1269–1273.
15. Wang, W.-W.; Zhu, Y.-J.; Yang, L.-X. ZnO−SnO_2 Hollow Spheres and Hierarchical Nanosheets: Hydrothermal Preparation, Formation Mechanism, and Photocatalytic Properties. *Adv. Funct. Mater.* **2007**, *17*, 59–64.
16. Yang, J.; Wang, D.; Han, H.; Li, C. Roles of Cocatalysts in Photocatalysis and Photoelectrocatalysis. *Acc. Chem. Res.* **2012**, *46*, 1900–1909.
17. Lim, B.; Jiang, M.; Camargo, P. H. C.; Cho, E. C.; Tao, J.; Lu, X.; Zhu, Y.; Xia, Y. Pd-Pt Bimetallic Nanodendrites with High Activity for Oxygen Reduction. *Science* **2009**, *324*, 1302–1305.
18. Tian, N.; Zhou, Z.-Y.; Sun, S.-G.; Ding, Y.; Wang, Z. L. Synthesis of Tetrahexahedral Platinum Nanocrystals with High-Index Facets and High Electro-Oxidation Activity. *Science* **2007**, *316*, 732–735.
19. Lauritsen, J. V.; Kibsgaard, J.; Helveg, S.; Topsøe, H.; Clausen, B. S.; Lægsgaard, E.; Besenbacher, F. Size-Dependent Structure of MoS_2 Nanocrystals. *Nat. Nanotechnol.* **2007**, *2*, 53–58.
20. Thurston, T. R.; Wilcoxon, J. P. Photooxidation of Organic Chemicals Catalyzed by Nanoscale MoS_2. *J. Phys. Chem. B* **1999**, *103*, 11–17.
21. Xiang, Q.; Yu, J.; Jaroniec, M. Synergetic Effect of MoS_2 and Graphene as Cocatalysts for Enhanced Photocatalytic H_2 Production Activity of TiO_2 Nanoparticles. *J. Am. Chem. Soc.* **2012**, *134*, 6575–6578.
22. Coehoorn, R.; Haas, C. Electronic Structure of $MoSe_2$, MoS_2, and WSe_2. II. The Nature of the Optical Band Gaps. *Phys. Rev. B* **1987**, *35*, 6203–6206.
23. Zong, X.; Yan, H.; Wu, G.; Ma, G.; Wen, F.; Wang, L.; Li, C. Enhancement of Photocatalytic H_2 Evolution on CdS by Loading MoS_2 as Cocatalyst under Visible Light Irradiation. *J. Am. Chem. Soc.* **2008**, *130*, 7176–7177.
24. Vinodgopal, K.; Kamat, P. V. Enhanced Rates of Photocatalytic Degradation of an Azo Dye Using SnO_2/TiO_2 Coupled Semiconductor Thin Films. *Environ. Sci. Technol.* **1995**, *29*, 841–845.
25. Wang, X.; Feng, H.; Wu, Y.; Jiao, L. Controlled Synthesis of Highly Crystalline MoS_2 Flakes by Chemical Vapor Deposition. *J. Am. Chem. Soc.* **2013**, *135*, 5304–5307.
26. Liu, Y.; Nan, H.; Wu, X.; Pan, W.; Wang, W.; Bai, J.; Zhao, W.; Sun, L.; Wang, X.; Ni, Z. Layer-by-Layer Thinning of MoS_2 by Plasma. *ACS Nano* **2013**, *7*, 4202–4209.
27. Liu, K.-K.; Zhang, W.; Lee, Y.-H.; Lin, Y.-C.; Chang, M.-T.; Su, C.-Y.; Chang, C.-S.; Li, H.; Shi, Y.; Zhang, H.; *et al.* Growth of Large-Area and Highly Crystalline MoS_2 Thin Layers on Insulating Substrates. *Nano Lett.* **2012**, *12*, 1538–1544.
28. Mak, K. F.; Lee, C.; Hone, J.; Shan, J.; Heinz, T. F. Atomically thin MoS_2: A New Direct-gap Semiconductor. *Phys. Rev. Lett.* **2010**, *105*, 136805.
29. Frindt, R. F.; Yoffe, A. D. Physical Properties of Layer Structures: Optical Properties and Photoconductivity of Thin Crystals of Molybdenum Disulphide. *Proc. R. Soc. London, Ser. A* **1963**, *273*, 69–83.
30. Wilcoxon, J. P.; Newcomer, P. P.; Samara, G. A. Synthesis and Optical Properties of MoS_2 and Isomorphous Nanoclusters in the Quantum Confinement Regime. *J. Appl. Phys.* **1997**, *81*, 7934–7944.
31. Chikan, V.; Waterland, M. R.; Huang, J. M.; Kelley, D. F. Relaxation and Electron Transfer Dynamics in Bare and DTDCI Sensitized MoS_2 Nanoclusters. *J. Chem. Phys.* **2000**, *113*, 5448–5456.
32. Chikan, V.; Kelley, D. F. Size-Dependent Spectroscopy of MoS_2 Nanoclusters. *J. Phys. Chem. B* **2002**, *106*, 3794–3804.
33. Mai, C.; Barrette, A.; Yu, Y.; Semenov, Y. G.; Kim, K. W.; Cao, L.; Gundogdu, K. Many-Body Effects in Valleytronics: Direct Measurement of Valley Lifetimes in Single-Layer MoS_2. *Nano Lett.* **2014**, *14*, 202–206.
34. Shi, H.; Yan, R.; Bertolazzi, S.; Brivio, J.; Gao, B.; Kis, A.; Jena, D.; Xing, H. G.; Huang, L. Exciton Dynamics in Suspended Monolayer and Few-Layer MoS_2 2D Crystals. *ACS Nano* **2013**, *7*, 1072–1080.
35. Wang, Q.; Ge, S.; Li, X.; Qiu, J.; Ji, Y.; Feng, J.; Sun, D. Valley Carrier Dynamics in Monolayer Molybdenum Disulfide from Helicity-Resolved Ultrafast Pump−Probe Spectroscopy. *ACS Nano* **2013**, *7*, 11087–11093.
36. Huang, X.; Zeng, Z.; Bao, S.; Wang, M.; Qi, X.; Fan, Z.; Zhang, H. Solution-Phase Epitaxial Growth of Noble Metal Nanostructures on Dispersible Single-layer Molybdenum Disulfide Nanosheets. *Nat. Commun.* **2013**, *4*, 1444.